Earth, Moon, and Planets (2005) 97: 213–231
DOI 10.1007/s11038-006-9100-z

Dust Production from the Hypervelocity Impact Disruption of Hydrated Targets

G. J. FLYNN
Department of Physics, State University of New York–Plattsburgh, 101 Broad St., Plattsburgh, NY 12901, USA
(E-mail: george.flynn@plattsburgh.edu)

D. D. DURDA
Southwest Research Institute, 1050 Walnut Street Suite 400, Boulder, CO 80302, USA

L. E. SANDEL, M. M. STRAIT
Department of Chemistry, Alma College, Alma, MI 48801, USA

(Received 15 November 2005; Accepted 23 June 2006)

Abstract. More than half of the C-type asteroids, which are the dominant type of asteroid in the outer half of the main belt, show evidence of hydration in their reflectance spectra. In order to understand the collisional evolution of asteroids, the production of interplanetary dust, and to model the infrared signature of small particles in the Solar System it is important to characterize the dust production from primary impact disruption events, and compare the disruption of hydrous and anhydrous targets. We performed impact disruption experiments of three "greenstone" targets, a hydrothermally metamorphosed basalt, and compared the results of these disruptions to our previous disruption experiments on porous, anhydrous basalt targets and to literature data on the disruption of non-porous, anhydrous basalt targets. The greenstone targets were selected because their major hydrous alteration phase is serpentine, the same hydrous alteration phase found in hydrous CM meteorites, like Murchison. The porous, anhydrous basalt targets were selected because their structure, consisting of millimeter-size olivine phenocrysts in a more porous, anhydrous matrix is similar to the structure of anhydrous chondritic meteorites, which consist of millimeter-size olivine chondrules embedded in a more porous, anhydrous matrix. The disruption measurements indicate the threshold collisional specific energy, Q^*_D, is 570 J/kg for the greenstone, which is lower than the literature values for non-porous basalt targets, and significantly lower than the value of 2500 J/kg that we have measured for porous anhydrous basalt targets. We determined the mass-frequency distribution of the debris from the disruption of the greenstone targets, which ranged in mass from 80 to 280 g, over a nine order-of-magnitude mass range, from ~10^{-9} g to the mass of the largest fragment. The cumulative mass-frequency distribution from the greenstone targets is fit by two power–law segments, one for masses $> 10^{-2}$ g, which is significantly steeper than the corresponding segment from the disruption of similar-sized anhydrous basalt, and one in the range from 10^{-9} to 10^{-2} g, which is significantly flatter than the corresponding segment from the disruption of similar size anhydrous basalt. These hydrous greenstone targets overproduce small fragments (10^{-4} to 10^{0} g) compared to anhydrous basalt targets, but underproduce dust-size grains (10^{-9} to 10^{-4} g) compared to anhydrous basalt targets.

Keywords: asteroids, cratering, disruption, hydrated targets, interplanetary dust, meteorites, micrometeorites

1. Introduction

The asteroid belt is compositionally zoned, with the inner half being dominated by high-albedo asteroids classified as S-type, while the outer half is dominated by low-albedo asteroids classified as C-, P-, or D-types, based on their reflection spectra (Gradie et al., 1989). The S-type asteroids are generally anhydrous, based on the absence of water features in their reflection spectra (Rivkin et al., 2002). The low-albedo C-, P-, and D-type asteroids, which dominate the outer half of the main-belt, are believed to be the parent bodies of many of the carbonaceous chondrite meteorites. Thus, these asteroids are likely to have similar physical properties to the carbonaceous chondrite meteorites. Many of the carbonaceous chondrite meteorites are hydrated, and many of the C-type asteroids show evidence for hydration in their reflection spectra. Among the C-type, main-belt asteroids for which visible-near-IR reflection spectra are available, 63% show the 3 μm adsorbed water band and 44% show the 0.7 μm hydroxyl band (Rivkin et al., 2002). Thus, a significant fraction of the targets for cratering and collisional disruption in the outer half of the main-belt are likely to be hydrated bodies.

Collisions are believed to be the dominant mechanism for dust production, surface erosion, and catastrophic disruption in the main-belt. In order to understand the collisional evolution of asteroids and interplanetary dust and to accurately model the infrared signature of small particles in our own Solar System and in other planetary systems, it is critical to address the fundamental problem of dust production from primary impact disruption events over a wide range of fragment sizes. At present, however, the size-frequency distribution for collision fragments is well-understood only within a few orders of magnitude of the size scale of the original target body. For impact disruption events at all size scales we still know very little about the primary production of fragments many orders-of-magnitude smaller than the original target body size. Thus, existing modeling results in these areas have large uncertainties.

Tomeoka et al. (2003) performed shock-recovery experiments, a technique in which a sample is shocked to known, high pressure and the microstructural and mechanical property effects are characterized quantitatively. They shocked a small target of Murchison, a hydrated carbonaceous chondrite meteorite, to pressures ranging from 4 to 49 GPa, and they compared the results to similar shock-recovery experiments on Allende, an anhydrous carbonaceous chondrite meteorite. Their examination of the Murchison samples a shows an abundance of local fractures, and the onset of this fracturing occurred at a significantly lower shock pressure than in Allende (Tomeoka et al., 2003). They further suggested that in porous materials the kinetic energy of the projectile is more effectively partitioned into heating, and that an effect of heating on hydrous targets would be the dehydration of

hydrous minerals and evaporation of H_2O, which would increase the gas volume and "contribute to generation of great expansive force on pressure release" (Tomeoka et al., 2003). As a result, they suggested that the hydrated asteroids would respond significantly differently to cratering and disruption than anhydrous asteroids. In particular, since the response of Murchison to shock facilitated the production of a dense array of fractures in the matrix, they proposed that impacts onto hydrated asteroids might contribute far fewer large objects and far more dust to the interplanetary medium then would be produced by anhydrous asteroids impacted under the same conditions. The conclusions reached by Tomeoka et al. (2003) have significant implications for the composition and mineralogy of the Zodiacal Cloud, the interplanetary dust particles (IDPs) collected by NASA from the Earth's stratosphere, and the micrometeorites collected from the polar ices.

In addition, Durda (1993) and Campo Bagatin et al. (1994) demonstrated that a sharp cutoff in the numbers of the smallest particles in a colliding population can induce significant wave-like deviations from conventional power-law size distributions, affecting even the largest bodies in the population. Thus, the size-frequency distribution of dust-size grains can influence the distribution of much larger, asteroid-size bodies.

However, the shock-recovery experiments performed by Tomeoka et al. (2003) only allowed them to observe the 2-dimensional distribution of local flaws induced by the shock, not the 3-dimensional distribution, which is necessary to demonstrate that a grain is actually free to separate from the host. Further, they did not actually observe the production of dust from their samples. A detailed knowledge of the response of both the hydrous and the anhydrous asteroids to impacts is required to understand the evolution of the main-belt and the production of dust in the Solar System. Nonetheless, many disruption experiments on naturally-occurring rock targets, designed to simulate asteroid dust production, cratering, or collisional disruption, have concentrated on anhydrous rocks, such as basalts.

We have previously conducted a series of impact disruption experiments on porous, inhomogenous terrestrial basalt targets (Durda and Flynn, 1999) and on anhydrous meteorites (Flynn and Durda, 2004) at the NASA Ames Vertical Gun Range (AVGR). In these experiments we directly monitor the production of the dust from our targets. By combining measurements of dust penetrations of foils located around the target, which measure the impact debris down to tens of microns in size, with the mass-frequency distribution of the larger fragments which we weigh after recovery of the debris from the floor of the AVGR chamber, we are able to determine the mass-frequency distribution of the debris over about a nine to ten order-of-magnitude mass range from $\sim 10^{-9}$ g to the mass of the largest fragment produced in the disruption.

The Hawaiian porphoritic olivine basalt targets, consisting of millimeter-size olivine phenocrysts in a fine-grained vesicular matrix, which were employed in our first experiments, were intended to crudely simulate anhydrous chondritic meteorites, which have millimeter-size olivine chondrules embedded in a more-porous, fine-grained matrix, and to simulate the asteroids that are parent bodies of the anhydrous chondritic meteorites (Durda and Flynn, 1999). We also disrupted nine anhydrous meteorite targets, eight ordinary chondrite meteorites and the carbonaceous chondrite Allende (Flynn and Durda, 2004). We have recently disrupted three hydrated targets at the AVGR (Flynn and Durda, 2005) in a preliminary assessment of the mass-frequency distribution of the dust produced by hypervelocity impacts into hydrous targets. In this paper, we compare the results on these three hydrous greenstone targets to our previous disruption experiments on the anhydrous Hawaiian basalt targets.

2. Samples and Techniques

In our earlier experiments we impacted five targets of anhydrous Hawaiian porphyritic olivine basalt. These targets ranged in mass from 67 to 674 g (see Table I). The bulk density was measured on three representative samples of the same Hawaiian basalt. We obtained values of 2.5, 2.6, and 2.7 g/cc for the three samples. Each of these values is significantly lower then the density of the minerals making up the rock (typically ~3.3 g/cc), demonstrating that our Hawaiian basalt targets exhibit significant porosity. Taking 3.3 g/cc as the density of non-porous basalt, we estimate the porosity of these Hawaiian vesicular basalt targets to be ~20%.

For the present experiment, we prepared targets of "greenstone," a basaltic rock in which the olivine and peridotite that made up the fresh rock have been metamorphosed by pressure and warm fluids into minerals including serpentine, epidote, actinolite, and chlorite, depending on the exact conditions of the alteration. Our samples were collected from a road cut along the California coast. Although they are not from the same location as the Hawaiian basalt targets employed in our previous experiments, we selected these greenstone targets because they are hydrothermally altered samples of a basaltic starting material. Since serpentine is a major alteration mineral in the CM carbonaceous chondrite meteorites, like Murchison, these targets were selected as a crude terrestrial analog to the hydrated meteorites.

The greenstone targets we employed appeared to be moderately fractured, which may affect its response to collisions. However, we note that most meteorites, including the hydrated carbonaceous meteorites, exhibit significant porosity (Flynn et al., 1999) and that the most common type of porosity in meteorites is cracks. Thus, the pre-existing fractures in our greenstone targets may make them suitable analog material for the hydrated asteroids.

TABLE I
Disruption conditions and results

Shot #	Target	Mass of Target (M_T) g	Projectile type[a]	Projectile speed km/s	Specific impact energy (Q) J/kg	Mass of largest fragment (M_L) g	M_L/M_T
030802	Greenstone	83	1/8-in Al	4.42–5.35[b]	6850	2.2	0.025
030805	Greenstone	229	1/8-in Al	4.86-4.93	2390	7.1	0.03
030810	Greenstone	492	1/8-in Al	3.93–3.95	720	227	0.46
961001	Anhyd. basalt	273	1/4-in Al	5.50	20060	2.9	0.011
961002	Anhyd. basalt	356.5	1/4-in Al	5.05	12950	5.8	0.016
961004	Anhyd. basalt	674	1/4-in Al	5.36	7720	17.9	0.027
011006	Anhyd. basalt	231	1/8-in Al	4.55	2040	141	0.61
011007	Anhyd. basalt	75.2	1/8-in Al	5.01	7610	20.5	0.27

[a]The 1/8-in Al projectiles had masses of 0.0452 to 0.0455 g, while the 1/4-inch projectiles had masses of 0.3620 g.
[b]Two different speed measurements differed significantly on this shot.

We impacted the three greenstone targets, weighing 83, 229, and 492 g, which spanned most of the range of masses of the anhydrous basalt target masses we had previously disrupted. The mean impact speed for asteroids in the main belt is ~5 km/s (Bottke et al., 1994), so we focused on shots with impact speeds in the 4–6 km/s range. In each of the greenstone disruptions, the projectile was a 1/8th inch diameter Al sphere fired at ~5 km/s using the NASA AVGR. This allowed us to examine the production of dust particles and the mechanics of fracture of the targets under the impact regimes that presently exist in the main asteroid belt.

The targets were each suspended at the center of the AVGR impact chamber. The target height was adjusted using a bore-site laser to center of the target along the path of the projectile. Each target was stabilized by a thin piece of fishing line running from the edge of the target to the floor of the AVGR chamber. This prevented rotation of the target when the chamber was pumped down to about 0.5 Torr before each shot, insuring that the projectile hit a relatively flat region of each target.

Four passive dust 'detectors,' consisting of thin aluminum foils (~7, 13, and 51 μm thick) mounted in 35 mm slide mounts, were placed around the target. Figure 1 shows two of the passive foil detectors in place in the AVGR chamber near one of Hawaiian basalt targets.

The Al foils were thin enough that small, high-speed particles would penetrate, providing a size distribution of high-speed, primary ejecta. The size of each hole in the foils was measured by scanning the entire area of a particular foil (equal to the window size of a standard 35 mm slide mount),

Figure 1. Anhydrous basalt target suspended in the AVGR chamber with two of the passive detectors, each containing two 7 μm, two 13 μm, and one 51 μm foils, deployed upstream from the impact. The projectile enters the AVGR chamber through the circular port in the top right of the image. In this case, a larger piece off Al-foil was deployed below the foil detector, to monitor the distribution of punctures over a larger area.

Figure 2. Slide scanner image of a 7-μm thick foil. This particular foil shows an unusually high number of penetrations because it intercepted a jet of debris from the disruption.

with either a Nikon slide scanner having a resolution of 2700 dpi or a Canon slide scanner having a resolution of 4000 dpi. The resulting 3894×2592 pixel images from the Canon slide scanner have a resolution of ~9.4 μm/pixel. Figure 2 shows one of the slide scanner images of a foil. Smaller sample areas of some foils were surveyed with a microscope/video setup at a resolution of ~1.6 μm/pixel. The size distributions of the holes in each foil were determined by analysis of the images with the software package ImageJ from NIH, which was used to determine the area of each hole and to convert that area to the diameter of a circular hole having the same area.

Following each shot, the debris was collected from the floor of the AVGR chamber. This process typically recovered $>95\%$ of the target mass. Large fragments (>0.02 g) that were collected from the chamber were individually weighed, allowing us to extend the size-frequency distribution to the largest masses from each fragmentation.

The impacts were recorded by either 500 fps or 1000 fps video. The details of each shot are summarized in Table I.

3. Results

The extent of the destruction in a collision is frequently characterized by the ratio of the mass of the largest fragment produced in the collision (M_L) to the mass of the target (M_T). This parameter, M_L/M_T, is 1 for a perfect rebound in which the target emerges unaltered. An M_L/M_T value of 0.5 is generally taken as the boundary between cratering events and catastrophic disruption (Fujiwara et al., 1989), with M_L/M_T ranging from 0.5 to 1 for cratering events, and $M_L/M_T \leq 0.5$ for catastrophic disruption. Each of the three greenstone targets suffered a catastrophic disruption, with the mass of the largest fragment being less than 50% of the target mass (see Table I). Four of

the five anhydrous basalt disruptions were also catastrophic. Two of the anhydrous basalt shots almost exactly mimicked the impact conditions experienced by two of the greenstone targets.

The anhydrous basalt Shot 011006 almost exactly mimicked the impact conditions of the greenstone Shot 030805. The mass of the anhydrous basalt target was 231 g compared to 229 g for the greenstone target. Both targets were struck by 1/8th inch diameter Al projectiles. The projectile speed was 4.55 km/s for the anhydrous basalt target and ~4.9 km/s for the greenstone target. Thus, the kinetic energy of the projectile was approximately 20% higher for the greenstone target. The greenstone target was much more severely disrupted than the olivine basalt target. The largest fragment from the olivine basalt disruption was 141 g, and the collision was not quite catastrophic since the mass of the largest fragment was ~0.6 times the mass of the target. The greenstone disruption was super-catastrophic, with the largest fragment having a mass of 7.1 g, only ~0.03 times the mass of the target. The factor of 20 difference in the mass of the largest fragment in these two disruptions cannot be explained simply by the ~20% difference in kinetic energy of the projectile.

In the second case, the anhydrous basalt Shot 011007 almost exactly mimicked the impact conditions of the greenstone Shot 030802. The mass of the anhydrous basalt target was 75.2 g compared to 83 g for the greenstone target. Both targets were struck by 1/8th inch diameter Al projectiles. The projectile speed was 5.01 km/s for the anhydrous basalt target and ~5.0 km/s for the greenstone target. In this case, the kinetic energy of the projectile was approximately the same for both targets. Again, the greenstone target was much more severely disrupted than the olivine basalt target. The largest fragment from the anhydrous basalt disruption was 20.49 g, and the collision was catastrophic since the mass of the largest fragment was ~0.27 times the mass of the target. The greenstone disruption was super-catastrophic, with the largest fragment having a mass of 2.2 g, only ~0.025 times the mass of the target.

In both cases the largest fragment from the disruption of the hydrous greenstone target was an order-of-magnitude smaller than the largest fragment from the disruption of an anhydrous basalt target of approximately the same mass that was impacted by an Al-projectile of approximately the same kinetic energy. This order-of-magnitude difference in the mass of the largest fragment in each of these pairs of disruption experiments indicates a substantial difference in the response of the hydrous greenstone and the anhydrous basalt targets to hypervelocity impact.

3.1. Size distribution from sieve-sorting

Disruption is a statistical process, so it is unlikely that disruption experiments on two similar targets impacted by similar projectiles will result in the largest

fragment having the same mass in both cases. The details of the disruption depend critically on many factors, including the distribution of flaws within the target, the detailed shape of the target, and the exact impact position of the projectile on the target. To minimize this statistical effect it is preferable to examine the entire distribution of fragments that are produced in the disruption, rather than focusing on the mass of the largest fragment. A target that exhibits enhanced production of dust must have a steeper slope of the cumulative mass-frequency distribution of the debris, reflecting the over-production of small fragments and the underproduction of larger fragments, than a target exhibiting normal dust production. However, at some size the cumulative mass-frequency distribution must flatten because the total mass of the fragments must sum to no more then the mass of the target plus the impactor. The size at which this flattening occurs determines if the disruption of this target makes a significant contribution to the IDPs (~5 to 50 μm in size), to the particles in the size range that produce the bulk of the infrared emission (typically particles near 100 μm in size), and to the micrometeorites (~50 μm to 1 mm in size).

The first step in determining the size-frequency distribution from each of the greenstone disruptions was to size-sort the material through a series of calibrated sieves – having holes of 4, 2, 1, 0.5, 0.25, 0.125, and 0.063 mm. The mass of material collected on each sieve was determined, and then the larger fragments, those having masses >0.02 g, were individually weighed.

The sieve data for the hydrous greenstone targets is tabulated in Table II. We recovered 95% of the target mass from Shot 030802 and 96% of the target mass from Shot 030805. The particles captured in the aerogel cells are

TABLE II
Mass on each sieve

Sieve	030802	030805
4 mm	29.0235 g	135.2279 g
2 mm	19.5353 g	37.4551 g
1 mm	13.2992 g	21.1157 g
0.5 mm	7.4043 g	2.6766 g
0.25 mm	4.5478 g	1.3719 g
0.125 mm	2.9608 g	4.3456 g
0.063 mm	2.3402 g	1.0918 g
Bottom tray	0.9086 g	1.0918 g
Recovered mass	79.198 g	220.663 g
Target mass	83 g	229 g
Recovered fraction	95.4%	96.3%

not included in the recovered mass, but the total mass of particles in the aerogel is $<<1$ g for each shot.

Data from disruption experiments is customarily plotted as a cumulative mass-frequency distribution. For material of uniform density, the volume is directly proportional to the mass. In order to directly compare the sieve data to data in cumulative mass-frequency distribution plots, we use the cube of the sieve size, which approximates the volume of the particles that were trapped on that sieve but passed through the next largest sieve, as a proxy for the mass of the particles. The material that passed through the smallest sieve (0.063 mm) was collected in the bottom tray and weighed as well. This material spans the size range from <0.063 mm to the smallest particle collected from the fragmentation. Since only a small fraction of the target mass was collected on the bottom tray, the plot of the cumulative mass-frequency distribution is not effected significantly by the choice of size for this sieve fraction. We have plotted it at a position that corresponds to the next smallest sieve size (0.031 mm). In addition, we included the largest fragment on the plot, inferring an equivalent sieve size from the measured mass of the largest fragment, assuming a density of 2.3 g/cc (the density of saponite), and calculating the side-length of a cube of the measured mass.

The cumulative mass-frequency plots are shown for two greenstone targets, Shot 030805 in Figure 3 and Shot 030802 in Figure 4. Both shots show the same trend, with very steep slopes for the largest fragments produced in the disruption, but rather shallow slopes for the small fragments. The transition from the steep to the shallow slope occurs at a cube of the sieve size of ~20 mm^3, which corresponds to a size of ~2.7 mm (or a mass of ~0.054 g, assuming a density of 2.7 g/cc for the greenstone).

Since the material that we sieved was collected from the floor of the AVGR chamber after each shot, there are several effects that could modifiy the mass-frequency distribution. First, some of the primary debris from the disruption strikes the walls or floor of the AVGR chamber at considerable

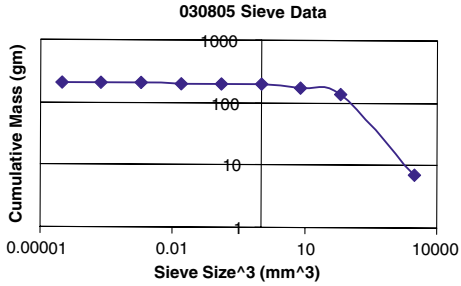

Figure 3. Cumulative mass-frequency distribution derived from sieve data for the disruption of greenstone target 030805. There is a change in the slope of the distribution near 20 mm^3.

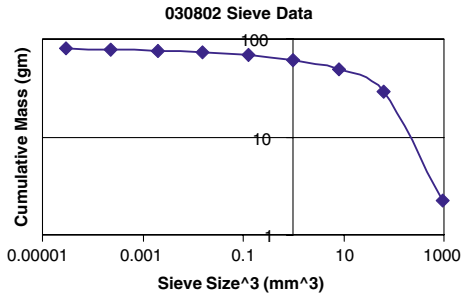

Figure 4. Cumulative mass-frequency distribution derived from sieve data for the disruption of greenstone target 030802. There is a change in the slope of the distribution near 20 mm^3.

speed, which might further break up the fragments. Second, the process of gently sweeping up the sample, as well as any rubbing of the fragments on one another during transport from the NASA Ames Research Center to the site of the sieving and weighing could produce further breakup. Both of these processes would produce more fine material. However, since we recover only ~95% of the mass of each target, it is possible that we are unable to efficiently recover some of the smallest particles from the floor of the AVGR chamber. To eliminate all of these possible effects, we deployed passive foil detectors, which record punctures from hypervelocity fragments, in positions around the target in the AVGR chamber.

3.2. Mass-frequency distribution of the fragments

We measured the size-frequency distribution of the holes in the 7, 13, and 51 micrometer thick foils placed in four locations around the target as well as the mass-frequency distribution of the larger fragments recovered from the floor of the AVGR chamber, individually weighing all of the particles down to a mass of 0.02 g.

Ideally, each target would have been completely surrounded by foil, documenting the size-frequency distribution of the fragments over the full 4π geometry. However, this in not practical, since the foil must be rigidly supported to minimize tearing from low-speed punctures. Further, it is not practical to count the penetrations in such a large area of foil. So, we mounted four foil detector arrays, like those shown in Figure 1, in positions around the target, two upstream and two downstream of the target.

Each of the foils was mounted in a 35 mm slide mount, with an exposed area of 8.05 cm^2. In order to combine the scanner data from the individual foils, each of which was mounted on up to four passive detector arrays placed at various distances from the target, the area of each individual foil is normalized to its projected area on a virtual 1-m radius sphere centered on the

target. The ratio of the surface area of the virtual 1-m radius sphere (125,664 cm^2) to the total projected area covered by all the foils for each shot is the correction factor used to scale the foil data to full 4π steradians.

The foil hole data were converted to particle diameters using the calibration data of Horz et al. (1995), presented in their Figure 14. We assume a particle speed of 2 km/s, the slowest of the impact speeds we measured by determining the time interval between the impact and the deflection of the detector observed in the high-speed video of each impact. The foil penetration data begins to flatten at a fragment size about twice the thickness of the foil, as expected, since our typical craters are bowl-shaped with depths that are about one-half their width. To generate a cumulative mass-frequency distribution it was then necessary to convert the particle diameter to particle mass. This was done by assuming densities of 2 and 3 g/cc, which bracket the density of saponite (2.3 g/cc), a major component of the hydrated targets, as well as the measured bulk density of the anhydrous basalt targets. Two sets of data points are shown for the foil data, one for each of the two density assumptions.

Figure 5 shows the composite mass-frequency distribution from the greenstone Shot 030805, combining the measurements from the foil penetrations and the individually weighed fragments. This composite mass-frequency distribution is consistent with the sieve data for this shot, shown in Figure 3. The data in Figure 5 is not well fit by a single power-law. The cumulative mass-frequency distribution of the fragments is best fit by two power-law segments, one having a slope of -0.17, covering the straight

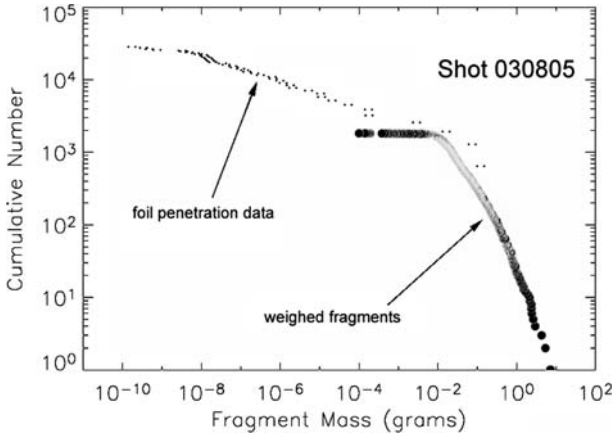

Figure 5. The composite cumulative mass-frequency distribution of the fragments from the disruption of a hydrous greenstone target (Shot 030805). The curve is best fit by two power-law segments, one having a slope of -0.17, covering the straight segment of the foil data, and the second having a slope of -0.94, covering the straight segment of the weighing data.

segment of the foil data, and the second having a much steeper slope of -0.94, covering the straight segment of the weighing data.

It is difficult to determine the transition size from Figure 5, because it occurs near the position where the two data sets are joined. The exact shape of the mass-frequency distribution in the transition region, from $\sim 10^{-4}$ g, where the foil data becomes unreliable because there are very few impacts at these large sizes into the very small area sampled by the foil, to $\sim 10^{-2}$ g, where the weighing data becomes unreliable because we may simply miss some of the particles because the selection of which particles are weighed is based on visual observation of their cross-section, is not determined. However the significant difference in the slopes between the two segments of the curve is readily apparent in Figure 5, and the transition occurs at a value consistent with the $\sim 5 \times 10^{-2}$ g determined from the sieve data for the same shot (Figure 3).

In comparison, Figure 6 shows the composite mass-frequency distribution from the disruption of an anhydrous basalt (Shot 011007). This cumulative mass-frequency distribution is reasonably well fit by a single power-law from the smallest masses that can be reliably detected by the foil penetration ($\sim 10^{-9}$ g) to at least 1 g, a nine order-of-magnitude mass range. The slope of the best fit to the power-law portion of the data is -0.72. There is some deviation from this power law at masses >1 g, with a noticeably steeper slope in this region. If we fit the foil and weighing data individually, the best-fit line to the foil data, covering the mass range from 10^{-4} to 10^{-9} g has a

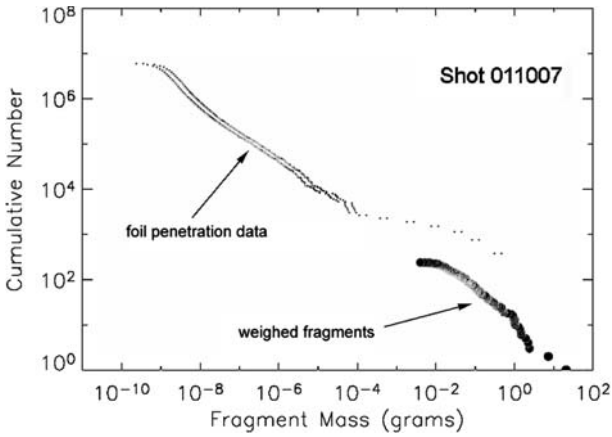

Figure 6. The composite cumulative mass-frequency distribution of the fragments from the disruption of an anhydrous basalt target. The curve can be fit by a single power-law with a slope of -0.72, but it is best fit by two power-law segments, one having a slope of -0.57, covering the straight segment of the foil data, and the second having a slope of -0.79, covering the straight segment of the weight data.

slope of -0.57 while the best fit line to the weighed fragments, for masses greater than 10^{-2} g, has a slope of -0.79.

The cumulative mass-frequency distribution from the greenstone disruption is significantly steeper for particles having masses $>10^{-2}$ g and significantly shallower for particles having masses $<10^{-4}$ g than the one from the disruption of the anhydrous basalt target, as shown in Figure 7. The best-fit lines to the two data sets show a significant overproduction of dust in the size range from 10^{-4} to 10^{0} g by the hydrous greenstone target compared to the anhydrous basalt target, but an underproduction of dust by the greenstone target at sizes smaller than 10^{-4} g.

We see the same trend in the foil data from all three greenstone disruptions, with each giving a very shallow slope in the 10^{-9} to 10^{-4} g range. The best-fit power-law to the foil data from greenstone shot 030802 (Figure 8) has a slope of -0.21, while the foils from greenstone shot 030810 (Figure 9) show a shallow continuous curve which we were unable to fit with a single power-law. The foil penetration data from the anhydrous basalt targets have much steeper mass-frequency distributions, with Shot 961001 being fit by a power law with a slope of -0.91 and Shot 011007 being fit by a power law with a slope of -0.57.

Thus, the greenstone targets produce dust with a very shallow slope in the mass-frequency distribution, while the anhydrous basalt produces foil penetrations with a much steeper size-frequency distribution. The implication is

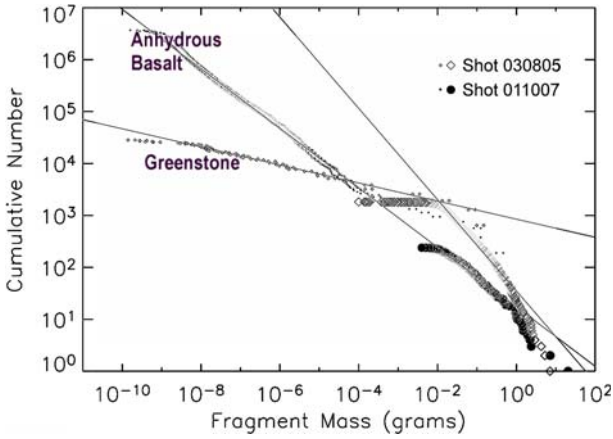

Figure 7. The composite cumulative mass-frequency distributions of the fragments from the disruption of an anhydrous basalt target (Shot 011007) and the hydrous greenstone target (Shot 030805). Both targets had approximately the same mass and were impacted by 1/8th-inch diameter Al-spheres having approximately the same kinetic energy. The best-fit lines to the two data sets show a significant overproduction of dust in the size range from 10^{-4} to 10^{0} g by the hydrous greenstone target compared to the anhydrous basalt target, but an underproduction of dust by the greenstone target at sizes smaller than 10^{-4} g.

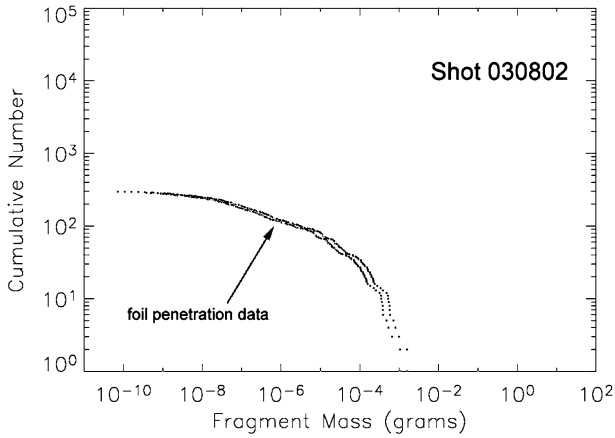

Figure 8. Cumulative mass-frequency distribution from the foil penetration data from Shot 030802.

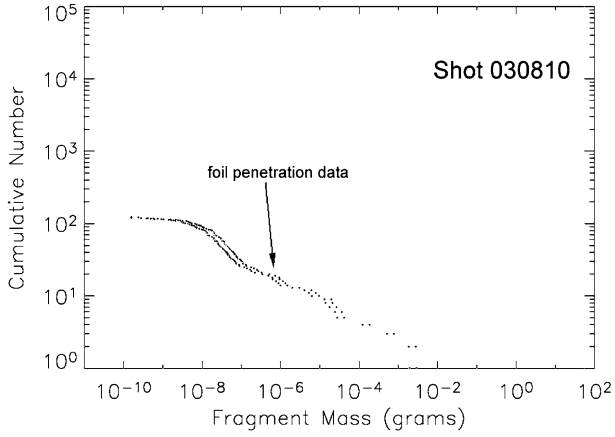

Figure 9. Cumulative mass-frequency distribution from the foil penetration data from Shot 030810.

that although the disruption of the greenstone produced an overabundance of fragments in the 10^{-4} to 10^{-0} g mass range, compared to the disruption of the anhydrous basalt, it produced fewer very small dust particles then the anhydrous basalt.

3.3. Q^*_D of the Targets

An alternative way to compare the disruption of these two different types of targets is to plot M_L/M_T versus the "specific impact energy," the impact

kinetic energy per unit target mass. These plots generally show a power-law trend in laboratory impact experiments on many terrestrial materials. The "threshold collisional specific energy," which is the energy required to disrupt the target material such that the largest fragment has 50% of the mass of the target (a parameter called Q^*_D) is then derived from the best fit to this power-law (as discussed by Fujiwara et al., 1989).

A plot of M_L/M_T versus the specific impact energy for the disruption of the three greenstone targets as well as M_L/M_T versus the specific impact energy data from our previous disruptions of the five anhydrous basalt targets is shown in Figure 10. A least squares fit to the three greenstone data points yields a value of 570 J/kg for Q^*_D. The fit to the five anhydrous basalt points yields a value of 2500 J/kg for Q^*_D.

There is considerable scatter in the data from both the anhydrous basalt and the greenstone targets, which results in a significant uncertainty in the inferred value of Q^*_D for each material. This scatter is expected for natural targets, since two targets of identical mass taken from the same source rock are likely to have differences in their shape, porosity, and flaw distribution, which contribute to different outcomes from the disruption. It is significant to note that each of the three greenstone disruptions plots well below the field defined by the anhydrous basalt target data points (see Figure 10), indicating that Q^*_D for the greenstone is significantly less than Q^*_D for the anhydrous basalt.

Similar impacts into nine anhydrous meteorite targets, previously reported in Flynn and Durda (2004), yield a value of 1419 J/kg for Q^*_D, while Fujiwara

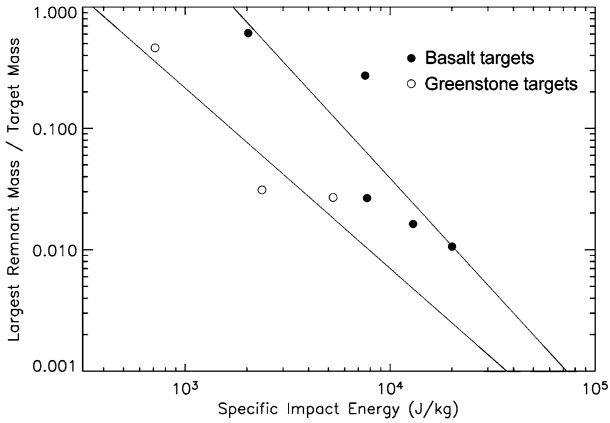

Figure 10. Plot of M_L/M_T versus specific impact energy for three greenstone targets and five porous, anhydrous basalt targets disrupted by ~5 km/s Al-projectiles. The threshold collisional specific energy, Q^*_D, derived from the best-fit to the greenstone data is 570 J/kg while the Q^*_D derived from the best-fit to the porous, anhydrous basalt data is 2500 J/kg.

et al. (1989) report that Q^*_D falls in the range from ~700 to 800 J/kg for collisions into non-porous glass, basalt, and granodiorite targets.

These results indicate that, at the size scale of ~200 g targets employed in this study, disruption of the hydrous greenstone targets requires less specific energy than is required to disrupt either porous or non-porous anhydrous basalt targets. Love et al. (1993) have shown that it requires more energy to disrupt a porous target than a non-porous one. Thus, the higher energy required for disruption of our Hawaiian basalt targets most likely results from the high porosity (~20%) of this material. This result can be understood by noting that if the target is porous some of the kinetic energy of the impactor is dissipated by compressing the target, and this energy is unavailable to disrupt the target. Our three greenstone targets were moderately fractured when we collected them, so they may also be somewhat porous. Thus, it is likely that Q^*_D for an unfractured sample of the greenstone would be significantly lower than we measured in these experiments.

4. Conclusions

Our measurements on three greenstone targets indicate that the disruption of these hydrated targets requires less specific energy than the disruption of anhydrous targets. The mass of the largest fragment produced by the hydrous greenstone disruption was smaller, by an order-of-magnitude, then the mass of the largest fragment produced by a similar-size porous, anhydrous basalt disrupted under the same conditions.

The best fit to the hydrous greenstone data indicates a threshold collisional specific energy (Q^*_D) of 570 J/kg, while the best fit to the anhydrous basalt data indicates a Q^*_D of 2500 J/kg. This is consistent with the proposal advanced by Tomeoka et al. (2003) that impact heating results in dehydration, and the subsequent gas expansion results in an explosive disruption of the target. We have observed similar effects, which we attributed to explosive disruption, in the impact of closed-pore Styrofoam targets containing gases trapped in their pores (Durda et al., 2003). However, highly-focused experiments on well-characterized targets will be required to understand the exact mechanism responsible for the difference in Q^*_D between hydrous and anhydrous targets.

The mass-frequency distribution of the debris from the disruption of the hydrous greenstone targets, which ranged in mass from 80 to 280 g, is fit by two power–law segments, one for masses $> 10^{-2}$ g, which is significantly steeper than the corresponding segment from the disruption of similar-size anhydrous basalt, and one in the range from 10^{-9} to 10^{-4} g, which is significantly flatter than the corresponding segment from the disruption of similar size anhydrous basalt. This indicates that the disruption of the

hydrous greenstone produces an overabundance of fragments in the mass range from ~10^{-4} to ~10^{0} g, but underproduces dust particles, in the 10^{-9} to 10^{-4} g mass range, the mass of IDPs and micrometeorites, compared to the disruption of a similar size anhydrous basalt target under the same conditions.

This result differs from the result reported by Tomeoka et al. (2003), who performed shock-recovery experiments on the hydrous meteorite Murchison and the anhydrous meteorite Allende and observed the distribution of flaws in the matrix introduced by the shock. They indicated that local fractures were induced in the Murchison target at a lower pressure, and suggested the hydrated asteroids might overproduce dust compared to anhydrous asteroids. We note, however, that, in these shock recovery experiments, Tomeoka et al. (2003) only observed the 2-dimensional distribution of local fractures in the recovered samples, not the actual production of dust. Although we observed the actual mass-frequency distribution of the dust and fragments produced in the disruptions and we selected a terrestrial target material rich in serpentine, the common aqueous alteration mineral in Murchison, it is not clear that hydrated meteorites or their asteroidal parent bodies will fragment in the same manner as the hydrous greenstone we employed as our target. The greenstone consists of clay that appears to be well-ordered over the large size scale, while the meteorite matrix exhibits less long-range order. Thus, it is critical to perform disruption experiments on hydrous meteorite targets in order to develop a better understanding of the response of hydrated asteroids to collisions and to assess the rate of dust production from the hydrous asteroids, which are parent bodies of these meteorites.

Acknowledgements

This work was supported by a NASA Planetary Geology & Geophysics research Grant [NAG04GH06G]. The disruption experiments were performed at the NASA Ames Vertical Gun Range. We thank Chuck Cornelison, Donald B. Bowling, Donald M. Holt, Thomas F. Reddy, and Richard E. Smythe of the Ames Vertical Gun Range.

References

Bottke, W. F., Nolan, M. C., Greenberg, R. and Kolvoord, R. A.: 1994, *Icarus* **107**, 255–268.
Campo Bagatin, A., Cellino, A., Davis, D. R., Farinella, P. and Paolicchi, P.: 1994, *Planet. Space Sci.* **42**, 1079–1092.

Durda, D. D.: 1993, 'The collisional evolution of the asteroid belt and its contribution to the Zodiacal Cloud', PhD Thesis. University of Florida.

Durda, D. D. and Flynn, G. J.: 1999, *Icarus* **142**, 46–55.

Durda, D. D., Flynn, G. J. and van Veghten, T. W.: 2003, *Icarus* **163**, 504–507.

Flynn, G. J., Moore, L. B. and Klöck, W.: 1999, *Icarus* **142**, 97–105.

Flynn, G. J. and Durda, D. D.: 2004, *Planet. Space Sci.*, special issue ''Catastrophic Disruption of Small Solar System Bodies'' (edited by Patrick Michel, Dan Durda), **52**, 1129–1140.

Flynn, G. J. and D. D. Durda, 2005, 'Catastrophic Disruption of Hydrated Targets: Implications for the Hydrated Asteroids and for the Production of Interplanetary Dust Particles', *Lunar Planet. Sci.* XXXVI, Lunar and Planetary Institute, Houston, TX, CD-ROM, Abstract # 1152.

Fujiwara, A., Cerroni, P., Davis, D., Ryan, E., Di Martino, M., Holsapple, K. and Housen, K.: 1989, in R. P. Binzel, T. Gehrels and M. S. Matthews (eds.), *Asteroids II*, University of Arizona Press, Tucson, pp. 240–265.

Gradie, J. C., Chapman, C. R. and Tedesco, E. F.: 1989, in R. P Binzel, T. Gehrels and M. S. Matthews (eds.), *Asteroids II*, University of Arizona Press, Tucson, pp. 316–335.

Horz, F. Contalla, M. J., Bernhard, R. P., Cardenas, F., Davidson, W. E., Haynes, G., See, T. H. and Winkler, J. L.: 1995, 'Penetration Experiments in Aluminum 1100 Targets Using Soda-lime Glass Projectiles'. NASA Technical Memorandum 104813.

Love, S. G., Hörz, F. and Brownlee, D. E.: 1993, *Icarus* **105**, 216–224.

Rivkin, A. S., Howell, E. S., Vilas, F. and Lebofsky, L. A.: 2002, in W. F. Bottke Jr., A. Cellino, P. Paolicchi and R. P. Binzel (eds.), *Asteroids III*, University of Arizona Press, pp. 235–253.

Tomeoka, K., Kiriyama, K., Nakamura, K., Yamahana, Y. and Sekine, T.: 2003, *Nature* **423**, 60–62.